



The 28th Iranian Conference on
Optics and Photonics (ICOP 2022),
and the 14th Iranian Conference on
Photonics Engineering and
Technology (ICPET 2022).

Shahid Chamran
University of Ahvaz,
Khuzestan, Iran,
Feb. 1-3, 2022



بررسی جفت‌شدگی مد پلاسمونی در دو نانونوار طلا

محمدرضا حسن پور و مصطفی قربانزاده

دانشگاه حکیم سبزواری، دانشکده مهندسی برق و کامپیوتر، سبزوار

چکیده- در این مقاله، با استفاده از جفت‌شدگی دو نانونوار طلا، یک بستر جدیدی را برای تشخیص و تله‌اندازی نانوذرات پیشنهاد می‌دهیم که از پلاسمون‌های سطحی انتشاری تحصیر و تقویت شده با نیم‌رخ مد متفاوت بهره می‌برد. ما با استفاده از روش تفاضل محدود مد ویژه (FDE) به بررسی مدهای پلاسمونی که مابین دو نوار طلا جفت شده تحریک می‌شوند، می‌پردازیم. ما در این بررسی نشان می‌دهیم که در ساختار فلز-دی الکتریک-فلز ارائه شده، پروفایل مدهای پلاسمونی، ضریب شکست موثر و میزان تلفات، وابستگی زیادی به ماده تشکیل دهنده عایق (محیط حس‌کنندگی)، ابعاد ساختار و فرکانس تابشی منبع دارد.

کلید واژه- پلاسمون‌های سطحی، تلفات، جفت‌شدگی موجبر، سنسور نوری، ضریب شکست موثر.

Investigation of plasmonic mode Coupling of two Gold Nano-strips

Mohammad-reza Hasanpour and Mostafa Ghorbanzadeh

Faculty of Electrical and Computer Engineering, Hakim Sabzevari University, P.O. Box 397,
Sabzevar 9617976487, Iran.

m.ghorbanzadeh@hsu.ac.ir

Abstract- In this paper, by coupling two gold strips we propose a new platform for sensing and trapping nanoparticles that benefit from enhanced and confined propagating surface plasmons with different mode profiles. We study the plasmonic modes that can be excited between these two coupled gold strips by the Finite difference eigenmode (FDE) method. We show that, in this Metal-Insulator-Metal (MIM) structure, the plasmonic mode profiles, effective refractive index (n_{eff}), and loss factor, strongly depend on insulator material (or sensing medium), the dimension of the structure, and the illuminated source frequency.

Keywords: Effective refractive index, loss, opto-sensor, surface plasmons, waveguide coupling.

1. Introduction

Plasmons are the collective motion of free electrons in metals coupled with light that makes a variety of applications at the nano-scale range [1]. Excitation of plasmons for a metal such as gold (Au) can be realized by the momentum matching technique to create a localized and enhanced field at the visible range of the light spectrum [2]. Due to subwavelength waveguiding, light concentration beyond the diffraction limit, ultrafast response, high environmental sensitivity and, flexibility in design, surface plasmons attract more attention in developing different types of sensors [3] and especially optical tweezers for example based on the propagating surface plasmons on top of a single gold strip layer [4].

In this paper, by coupling two gold strips we propose a new platform for sensing and trapping nanoparticles that benefit from enhanced and confined propagating surface plasmons with different mode profiles. We study the plasmonic modes that can be excited between two coupled gold strips by the finite difference eigenmode (FDE) method. We show that, in this Metal-Insulator-Metal (MIM) structure, the plasmonic mode profiles, effective refractive index (n_{eff}), and loss factor, strongly depend on insulator material (or sensing medium), the dimension of the structure, and the illuminated source frequency.

2. Structure and simulation method

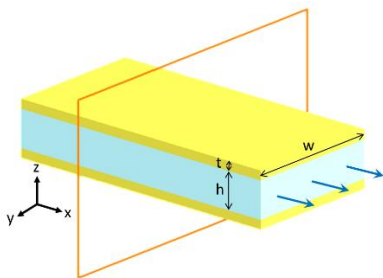


Fig. 1: The structure of coupled Gold strip

The coupled gold strip waveguide is made up of three main parts including a middle dielectric layer and top and bottom gold (Au) metal layers that are

shown in Fig. 1. The height of the middle dielectric layer, the thickness of the metal layer, and the width of the waveguide are indicated by h and t , and w , respectively. The frequency of the source (that will be injected along the $-x$ direction) is set to $36 \cdot \text{THz}$ ($\sim 833 \text{ nm}$), which is compatible with biological objects.

In Fig. 2(c) the y - z cross-section of the waveguide is illustrated. Here, the selected values for the dimensions are 50 nm , 200 nm and, 500 nm for t , h , and w , respectively. In these simulations, we have only considered the first five modes which had the highest n_{eff} . In Fig. 2(a)-(b), the vertical yellow line at the $h=200 \text{ nm}$ shows the effective index and loss factor of the waveguide by the mentioned h, w and, t values. the profile of the electric fields in both x and z directions (E_x and E_z), the real part, and the phase of the mentioned fields have been analyzed to distinguish and label them.

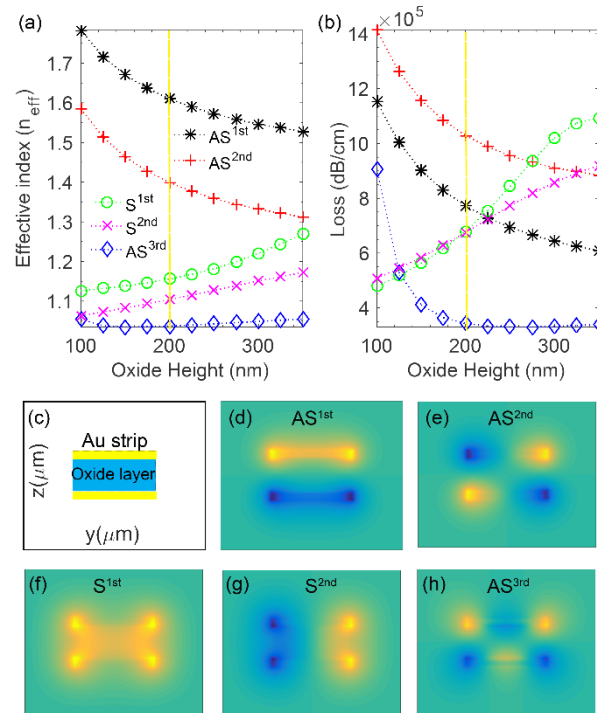


Fig. 2: (a)-(b) Effective refractive index and loss variations with varied dielectric height h . (c) Cross-section view of MIM waveguide at the y - z plane. (d)-(h) E profiles of MIM waveguide at the y - z plane. $w=500 \text{ nm}$, $h=200 \text{ nm}$ and $t=50 \text{ nm}$

3. Simulation and Results

The observed modes have been categorized based on the symmetry of the electric field respect to the y axis at the middle of the dielectric layer, in the y - z plane. Fig. 3(d)-(h) respectively shows the AS^{1st} , AS^{2nd} , AS^{3rd} , S^{1st} , and S^{2nd} modes in which S and AS represent the Symmetric and the Anti-symmetric modes and the superscript indicates the mode number. In the following sections the effect of waveguide dimensions, frequency, and insulating refractive index have been investigated.

3.1 Effect of dielectric height on the waveguide modes

In Fig. 3(a)-(b) we swept the height of the dielectric h between 100:300 nm with 20 nm steps meanwhile, the thickness of the Au layer t and the width of the structure w is remained constant at 50 nm and 100 nm, respectively. According to the simulations, the modes with higher n_{eff} (AS^{1st}) still can belong to the same category for a wider interval. The intervals we have selected in the figures are the maximum common valid range from the aspect of categorization. Hence, some of the modes may continue for a limited interval of the sweeping parameter. According to Fig. 3(b), it's noticeable that by increasing the oxide height h for the interval between 100 and 300 nm, the loss factor of the anti-symmetric modes decreases exponentially. In contrast, the loss factor of symmetric modes increase uniformly.

3.2 Effect of structure width on the waveguide modes

Fig. 3 (a)-(b) demonstrates the variations of the n_{eff} and $loss$ versus the structure width w . Referring to Fig. 3 (a), AS^{1st} has the highest n_{eff} among all other modes. All three anti-symmetric modes showed significant growth while widening the structure. However, the symmetric are converging to the value of $n_{eff}=1$. In the given range of w , the n_{eff} of the AS^{1st} , AS^{2nd} , and AS^{3rd} increase 0.1, 0.15, and 0.35, respectively. In contrast, the S^{1st} and S^{2nd} modes converge to 1.0 and 1.1, respectively.

of the loss of the waveguide. In this graph, the AS^{3rd} has the highest variation relative to all other modes.

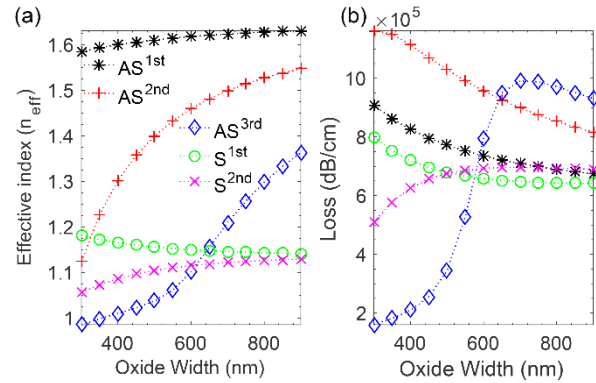


Fig. 3: (a)-(b) *Effective index and loss variations versus w when $h=200$ nm, $t=50$ nm, and $w=100$ nm with 20 nm steps, respectively.*

For this mode at $w=100$ nm, the $loss$ is as high as 9.9×10^5 dB/cm. AS^{1st} , AS^{2nd} , and S^{1st} has a decremental loss response during this period. S^{2nd} mode also has a gradual increase and saturates at 6.9×10^5 at the end of the interval.

3.3 Effect of metal layer thickness on the waveguide modes

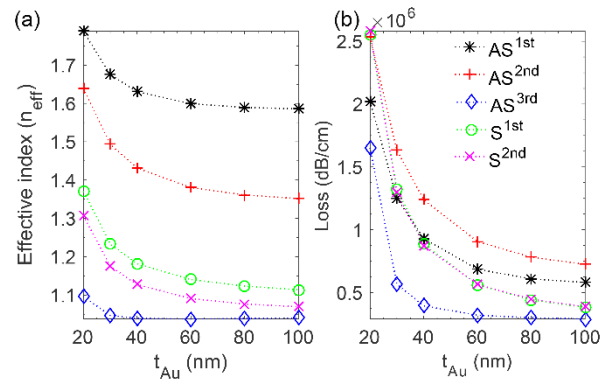


Fig. 4: (a)-(b) *Effective index and loss variations for $t=20$ nm, $h=200$ nm, and $w=100$ nm.*

In Fig. 4(a)-(b), we have demonstrated the effect of the metal layer thickness t on the n_{eff} and $loss$ of the channel. At the frequency of 36 THz and constant values of h, w , and RI of the middle layer, we swept t from 20 to 100 nm by 20 nm steps. It's noticeable that the amount of the n_{eff} and $loss$ has been decreased in all five modes over the variation interval of t . Based on the results AS^{2nd} mode has

the highest decrease of n_{eff} by a value of 0.247. In contrast, the AS^{rd} mode had the lowest decay by the value of 0.00 and remained approximately constant for the rest of the interval. Hence, the symmetric modes had the highest rate of decay of loss of around 2.1×10^{-1} up to the end of the interval. The AS^{rd} had the most rapid drop of loss for the interval of t between 20 and 30 nm.

3.4

In this simulation, we have changed the frequency f of the excited modes from 300 to 440 THz (~ 999 to 181 nm) with 20 THz steps. The graphs on Fig. 6(a)-(b) show the variation of n_{eff} and loss versus frequency. This leads to an increase in both n_{eff} and loss in all modes.

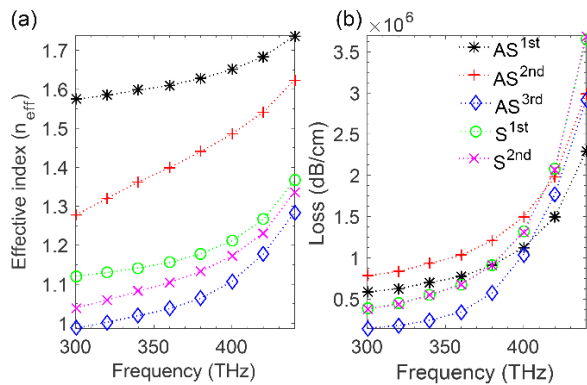


Fig. 6: (a)-(b) Effective index and loss variations. $h=20$ nm, $t=20$ nm, and $w=20$ nm. $f=300$ to 440 THz

According to Fig. 6(a), the n_{eff} of the AS^{rd} mode has the highest rate of variation of about 0.247 and it has approximately a linear response in the given range of f . According to Fig. 6(b), the S^{rd} and S^{1st} modes show high sensitivity to frequency changes due to the highest variation of the loss parameter of about 2.1×10^{-1} dB/cm. In contrast, the AS^{1st} mode shows the least changes in both n_{eff} and loss.

3.5

Fig. 7(a) illustrates the variation of n_{eff} when the refractive indices RI of sensing media changes. In this simulation, we have investigated the capability of the structure in sensing different target materials.

The RI s for the selected layer are 1.33, 1.40, 1.50, and 1.60 while all other parameters such as h , t , w , and f remained constant.

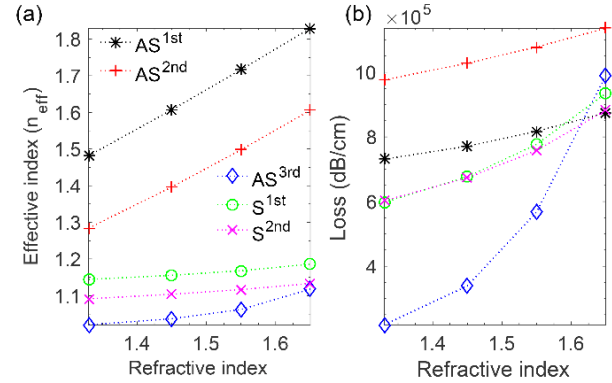


Fig. 7: (a)-(b) Effective index and loss variations versus RI for $h=20$ nm, $t=20$ nm, $w=20$ nm.

It's noticeable that by increasing the RI of the middle layer, the n_{eff} and loss increase (Fig. 7(a)-(b)). The AS^{1st} and AS^{rd} has the highest n_{eff} variation of about 0.247 and 0.247 respectively. The variations of these two modes are perfectly linear in both graphs. The loss graph also demonstrates that the AS^{rd} has the highest loss variation of about 2.1×10^{-1} dB/cm.

4. Conclusion

According to the simulation results, for the given MIM structure, the n_{eff} and loss strongly depend on the structure geometry, dielectric material, and injection mode frequency. By utilization of the proper mode profile and geometry optimization, a high sensitive Opto-sensor can be realized.

References

- [1] V. G. Kravets, A. V. Kabashin, W. L. Barnes and A. N. Grigorenko, "Plasmonic Surface Lattice Resonances: A Review of Properties and Applications," *Chemical Reviews*, vol. 118, no. 12, pp. 5912-5951, 2018.
- [2] R. A. Alvarez-Puebla, J.-F. Li and X. Y. Ling, "Introduction to advances in plasmonics and its applications," *Nanoscale*, vol. 12, no. 12, pp. 5930-5936, 2020.
- [3] A. I. Fernández-Domínguez, F. J. García-Vidal and L. Martín-Moreno, "Unrelenting plasmons," *Nature Photonics*, vol. 11, no. 1, pp. 8-10, 2017.

[۴] Y.-C. Lin and P.-T. Lee, “Efficient Optical Trapping
of Nano-Particle via Waveguide-Coupled Hybrid

Plasmonic Nano-Taper,” *IEEE Photonics Journal*,
vol. ۱۱, no. ۳, pp. ۱-۱۳, ۲۰۱۹.